Journal Name

Dynamic Article Links ►

Cite this: DOI: 10.1039/c0xx00000x

www.rsc.org/xxxxxx

EDGE ARTICLE

Holistic Approach to Dissolution Kinetics: Linking Direction-Specific Microscopic Fluxes, Local Mass Transport Effects and Global Macroscopic Rates from Gypsum Etch Pit Analysis

Massimo Peruffo[a], Michael M. Mbogoro[a], Martin A. Edwards[a,b] and Patrick R. Unwin[a]*

Received (in XXX, XXX) Xth XXXXXXXXX 20XX, Accepted Xth XXXXXXXXX 20XX
DOI: 10.1039/b000000x

Dissolution processes at single crystal surfaces often involve the initial formation and expansion of localized, characteristic (faceted) etch-pits at defects, in an otherwise comparatively unreactive surface. Using natural gypsum single crystal as an example, a simple but powerful morphological analysis of these characteristic etch pit features is proposed that allows important questions concerning dissolution kinetics to be addressed. Significantly, quantitative mass transport associated with reactive microscale interfaces in quiescent solution (well known in the field of electrochemistry at ultramicroelectrodes) allows the relative importance of diffusion compared to surface kinetics to be assessed. Furthermore, because such mass transport rates are high, much faster surface kinetics can be determined than with existing dissolution methods. For the case of gypsum, surface processes are found to dominate the kinetics at early stages of the dissolution process (small etch pits) on the cleaved (010) surface. However, the contribution from mass transport becomes more important with time due to the increased area of the reactive zones and associated decrease in mass transport rate. Significantly, spatial heterogeneities in both surface kinetics and mass transport effects are identified, and the morphology of the characteristic etch features reveal direction-dependent dissolution kinetics that can be quantified. Effective dissolution velocities normal to the main basal (010) face are determined, along with velocities for the movement of [001] and [100] oriented steps. Inert electrolyte enhances dissolution velocities in all directions (salting in), but a striking new observation is that the effect is direction-dependent. Studies of common ion effects reveal that Ca^{2+} has a much greater impact in reducing dissolution rates compared to SO_4^{2-}. With this approach, the new microscopic observations can be further analysed to obtain macroscopic dissolution rates, which are found to be wholly consistent with previous bulk measurements. The studies are thus important in bridging the gap between microscopic phenomena and macroscopic measurements.

a Electrochemistry and Interfaces Group, Department of Chemistry, University of Warwick, Coventry, CV4 7AL, UK. E-mail:p.r.unwin@warwick.ac.uk
b Molecular Organization and Assembly in Cells, Doctoral Training Centre, University of Warwick, Coventry, CV4 7AL, UK.

Cite this: DOI: 10.1039/c0xx00000x

www.rsc.org/xxxxxx

EDGE ARTICLE

Introduction

This paper introduces a simple, but powerful, approach for elucidating the rate of crystal dissolution, a process driven by undersaturation at the crystal/solution interface.[1, 2] In comparison to crystal growth, for which a wide body of experimental and theoretical data are available,[3, 4] the kinetics and mechanisms of crystal dissolution are less well understood and new features continue to emerge.[5, 6] At the most basic level, the reliable elucidation of dissolution kinetics (and interfacial kinetics in general) requires the determination of the relative contributions of mass transport (diffusion of dissolution products into bulk media) and surface reactions (processes resulting in the generation of soluble species at the crystal/solution interface).[1, 7]

Traditional methods for the study of crystal dissolution have tended to be macroscopic, such as batch and column experiments on particulates,[8, 9] as well as techniques that deliver well-defined mass transport, such as the rotating disk method,[10, 11] and channel flow cells.[12] More recently, microscopic and nanoscopic techniques such as atomic force microscopy (AFM),[8, 13, 14] scanning electrochemical microscopy (SECM)[15] and vertical scanning interferometry (VSI)[4, 16] have been used to probe dissolution processes at the local level. While undoubtedly having a significant impact in terms of phenomenological observation, *in situ* AFM dissolution studies are often limited to either very slow processes or close to equilibrium conditions (for fast processes) so that the reaction is compatible with the AFM time scale, thereby restricting the range of intrinsic kinetics accessible.[13] Furthermore, mass transport in AFM fluid cells, both at the nanoscale and macroscale,[17] is rather complex. It is noteworthy that it has not yet been possible to link nanoscale dissolution kinetics, from AFM, to more conventional macroscopic flux measurements: there is a significant kinetic gap (typically by at least an order of magnitude).[6]

Dissolution is often initiated on a crystal surface through the formation of etch pits at defect sites, giving rise to a heterogeneously active surface.[8, 18] The morphologies of such etch features have been analysed to reveal information about the mode of action of crystal habit modifiers and dissolution/growth inhibitors,[2,19] and dissolution kinetics for slow (surface-controlled) processes.[4b, 10, 20] In this paper we propose a powerful, but simple, quantitative analysis of plane-specific dissolution kinetics by measuring the dimensions of individual characteristic etch pits formed at dislocations on freshly cleaved surfaces as a function of short, well-defined times. By coupling these observations to a diffusion model, the importance of mass transport in dissolution can be elucidated readily, along with the evaluation of (plane-specific) interfacial concentrations and the deduction of direction-dependent kinetics. The inspiration for the analysis of microscopic features in this way comes, in part, from the field of ultramicroelectrodes (UMEs)[21] and ultramicroelectrode arrays[22] which have shown that fast surface kinetics and the relative importance of diffusion can be measured simply and effectively by shrinking the length scale of the reactive interface. In particular, UMEs have intrinsic mass transport rates that are much higher than can be achieved with convective systems. For example, diffusion rates to a 1 µm diameter electrode, with a typical diffusion coefficient of 10^{-5} cm^2 s^{-1} is about 10 times higher than a rotating disk electrode at a high rotation speed of 50 Hz (3000 rpm) assuming a typical kinematic viscosity of 0.01 cm^2 s^{-1}.[23] A further consequence of studying microscale interfaces is that they are relatively immune to convection, with steady quasi-hemispherical diffusion dominating.

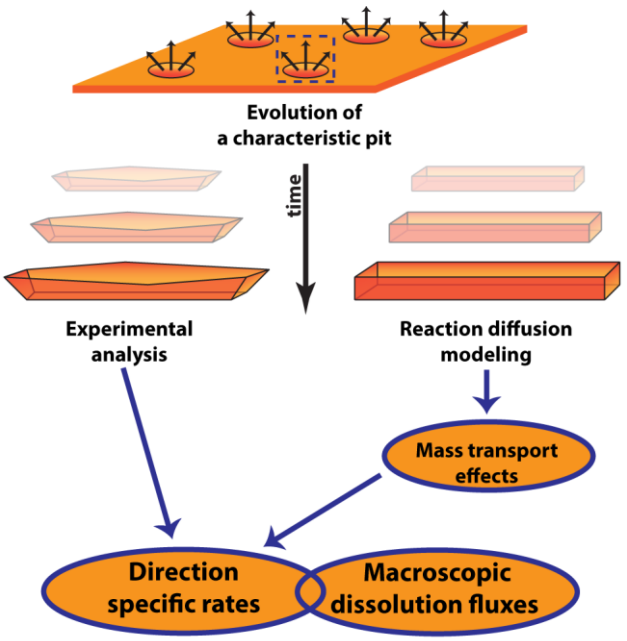

Fig.1 Schematic for etch pit analysis, in which a flat crystal surface is etched and dissolution is monitored by tracking the expansion of characteristic etch pits. Using complementary computer simulations to mimic the observed pit dynamics allows dissolution kinetics, surface concentrations and mass transport effects to be deduced.

Figure 1 illustrates the conceptual approach used, where characteristic etch pits on a surface, undergoing the initial stages of dissolution, are measured at selected etching times. With the time-dependent etch pit dimensions as an input, a simulation is developed which accurately describes local fluxes and diffusion processes and predicts interfacial concentrations. The approach yields molecular-level dissolution kinetics that may be linked readily to macroscopic fluxes, providing self-consistent hierarchical description of kinetics that closes the gap between the nanoscale and macroscale.

We have chosen to study gypsum single crystal, as an example of an abundant sedimentary mineral[24] with extensive

applications.[25-28] In its optically transparent form (selenite), gypsum exhibits a perfect cleavage with near atomic scale flatness along the (010) plane, which makes it particularly attractive for initial investigations with the proposed method. Various studies have explored gypsum dissolution at the macroscale[29, 30] and nanoscale,[31, 32] in some cases under close to equilibrium conditions.[31] Most nanoscale studies have reported the formation of shallow pits (pit depth ≈ 8Å). Some early studies highlighted the importance of mass transport[25, 26] while others indicate surface kinetic control.[27] Recent studies[30, 33] have suggested mixed-kinetics.

Despite this body of work, neither elementary direction-specific dissolution rates, nor common ion effects have been reported for gypsum dissolution. We recently reported the intrinsic dissolution kinetics of the basal (010) surface, but in studies of the edge plane orientation, i.e. the (100) or (001) surface, we found dissolution to proceed at a diffusion-controlled rate, even with the high mass transport rates accessible from a channel flow cell.[30] This serves to highlight the general difficulty of measuring fast dissolution kinetics even with quite sophisticated hydrodynamic techniques. The approach herein addresses these missing features, provides new intrinsic kinetic data for these fast moving planes, and leads to an holistic view of dissolution kinetics.

Experimental

Solutions

All solutions were prepared from ultrapure Milli-Q reagent grade water (Millipore) with a typical resistivity of 18.2 MΩ cm (25°C). Salt solutions, each with an ionic strength (IS) of ≈ 0.2 M were prepared using either: (i) 75 mM $Ca(NO_3)_2 \cdot 4H_2O$ (Sigma); (ii) 75 mM Na_2SO_4 (Fisher Scientific); or (iii) 0.2 M $NaNO_3$ (Aldrich). The IS and chemical speciation were calculated using the numerical code MINEQL+.[34, 35] Using this method, the solubility of gypsum, C_{sat} (total concentration of dissolved calcium at equilibrium) was found to be ≈ 16.2 mM in pure H_2O which compares well to the value reported experimentally (≈ 15.1 mM).[28] C_{sat} in the presence of $NaNO_3$ was calculated to be ≈ 32 mM.

Etch pit visualization and analysis

In order to enhance surface reflectivity, after each etching experiment (for a specific time), samples were sputtered with gold (Sputter Coater Quorum Technologies) producing a uniform coating ≈ 12 nm thick across the surface, which was negligible compared to the dimensions of the etch features. The resulting surfaces were visualized routinely via differential interference contrast (DIC) optical microscopy (Leica DM 4000, Leica Microsystems) and AFM (AFM-tapping mode™, using RFESP tips on a Veeco Multimode V with Nanoscope V Controller). Topographical images produced via AFM were analyzed via a Matlab program designed in-house.[36]

Etching of crystal surfaces

Large natural gypsum crystals in the form of selenite (St-Gobain Gyproc) were broken into manageable pieces (area ≈ 2 cm^2) and then cleaved along the (010) plane with a sharp razor blade, to produce clean fresh surfaces largely devoid of macrosteps. In some cases, the two surfaces produced were both studied and considered to be mirrors.[31] This provided a check that etch pits studied were those formed at dislocations running through (essentially perpendicular to) the (010) surface, thereby ensuring that all measurements were made at *characteristic pits* (see Etch pit visualization and analysis section). The samples were cleaned with a strong burst of ultrapure N_2 gas (BOC) to remove any adhered micro fragments. Next, they were mounted onto a holder with the (010) plane flush to the solution. In order to minimize contamination, samples were handled with tweezers at all times and only fresh cleavages were used.

Etching of individual crystals was carried out in approximately 100 ml of quiescent solution in a glass beaker. Experiments were performed at 24 ±1°C. A freshly cleaved mounted crystal sample was submerged into the solution of interest to achieve complete surface wetting. After a set time, the sample was withdrawn and immediately dried with a strong burst of N_2 gas. The drying took ≈ 3 seconds, which is significantly shorter (by at least an order of magnitude) than the etch process and thus may be viewed as an insignificant contribution to the etch duration. For the dissolution experiments in salt solutions, etched samples were quickly rinsed in water before drying with N_2 gas. This was done to minimize the precipitation of salts on the crystal surface, upon drying with N_2 gas. Again, this process did not significantly influence the etching process. Dissolution experiments were carried out for times in the range between 30 ±3 and 105 ±3 s. It was also important to determine that the surface adjacent to the pits was essentially inert on the time scale of the measurements herein, because this could alter the apparent depths and dimensions of pits measured. To this end, a section of prepared samples was masked off and protected with tape (Scotch™ pressure sensitive tape, 3M) which was carefully removed after dissolution.

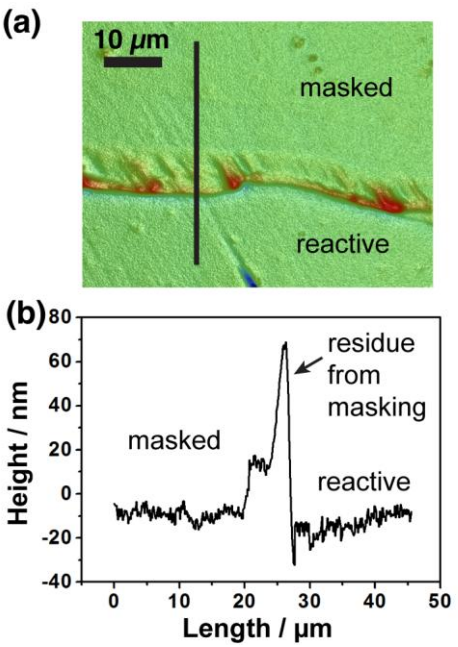

Fig. 2 (a) Typical vertical scanning interferometry micrograph of gypsum (010) surface after etching for 180 sec and (b) plot of cross-section across the surface between masked and reactive regions. Residue from the masking marks the boundary.

To locate the region of interest, the surfaces were then

visualized quantitatively via DIC microscopy, from which it was found that dissolution features stopped abruptly at the boundary between the masked-off region and the exposed crystal surface. The surfaces were visualized via vertical scanning interferometry (VSI, NT 2000 Surface Profiler, WYKO systems) at a number of places across this boundary so as to measure any global recession of the basal plane. Figure 2(a) shows a VSI micrograph of the gypsum (010) basal surface after etching for 180 s (longer than the studies in the paper) in pure H_2O. The irregular elevated region between the masked and reactive areas is residue left after removal of the masking tape. The residue allowed for a clear demarcation between the active and inactive regions over the surface. Figure 2(b) is a plot of the cross section shown in Figure 2(a), and highlights a negligible change in global height between the two regions. The average difference in height between the two regions was found to be < 10 nm after etching for 180 s. Since the maximum etching time for dissolution experiments was ≈ 100 s, we could therefore conclude that for the timescale chosen, dissolution was largely limited to the characteristic pits analysed. Most importantly, since the pit depths on this time scale were much more than an order of magnitude larger, we could reasonably assume an inert basal surface for the purpose of analysing pit dimensions.

Theory and simulations

A mass transport model was designed, which prescribed the internal pit surface as a function of time, according to experimental data. The analysis revealed spatially-resolved dissolution fluxes from which local interfacial concentrations were determined. As described herein, this allowed the deduction of the kinetic regime (mass transport control, surface kinetic control, or mixed kinetics/mass transport) and the elucidation of the contributions of dissolution rates in specific directions. Ultimately, the relative contributions of microscopic values to the overall macroscopic measurements were elucidated. Numerical simulations were executed on a Dell Intel core™ 2 Quad 2.49 GHz computer equipped with 8 GB of RAM and running Windows XP Professional X64 bit 2003 edition. Modelling was performed using the commercial finite element modelling package Comsol Multiphysics 3.4 (Comsol AB, Sweden), using the Matlab interface. Simulations were carried out with > 27 000 tetrahedral mesh elements and mesh resolution was defined to be finest in the vicinity of the etch pit. Simulations with finer meshes were carried out to confirm that the mesh was sufficiently fine to ensure that the predicted solutions were accurate.

The finite element domain shown schematically in Figure 3(a, b) was used, which approximated the pit reasonably to the monoclinic geometry of the gypsum unit cell and the dimensions of a typical pit at a specific time.

Due to the steep tapering of the experimental etch pit walls, the lateral pit dimensions used for simulations were approximated to the experimental pit dimensions (Figure 3(c)) taken at 50% pit depth, while pit depth was taken from average depth of the pit (010) face. In addition, the pit profile in the [001] direction (pit length) reasonably followed this geometry (Figure 3(d)). It was assumed that the distance between etch pits was sufficiently large to avoid overlap of concentration boundary fields between adjacent pits. This assumption is reasonable for the timescale we chose to analyse, coupled with the fact that it was found that the reaction was far from diffusion-control (*vide infra*). The model could easily be developed to allow for diffusional interaction of material from neighbouring pits if needed in the future.

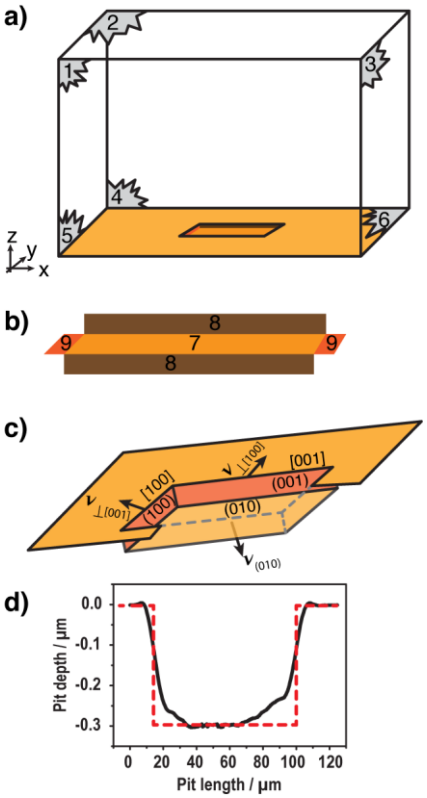

Fig. 3 (a) Simulation domain used for finite element simulations of plane (direction)-specific dissolution fluxes where the numbers represent the boundaries used in simulations (not to scale). (b) The simulated etch pit whose walls have been opened up for clarity and (c) etch pit planes and directions of step motion are shown. (d) Cross section of a pit along the length ([001] direction). The dashed line represents the approximation used for the pit geometry.

We describe mass transport of ions from the crystal surface to bulk solution by the stationary diffusion equation solved with boundary conditions defined below:

$$D_i \nabla^2 C_i = 0 \qquad (1)$$

where D_i is the diffusion coefficient of species i, where i is Ca^{2+} or SO_4^{2-}, and C_i is the concentration of species i. The use of equation 1 assumes that the expansion of the pit is slow compared to the characteristic diffusion times, $t_{diff} \approx l_p^2 / D_i$, where l_p is the characteristic pit dimension. For all of the cases herein, this condition was satisfied. Dissolution of ions from the crystal surface was considered to be a stoichiometric process so that electroneutrality was maintained. As shown herein, the dissolution reaction at short times occurs under driving conditions where dissolving species are rapidly transported from the reactive interface. To simplify the problem, we reasonably carried out a one species simulation using an average diffusion coefficient D_i = 0.94 ×10^{-5} cm^2 s^{-1} (0.79 ×10^{-5} cm^2 s^{-1} and 1.07 ×10^{-5} cm^2 s^{-1},[37] diffusion coefficients for Ca^{2+} and SO_4^{2-}, respectively).

The walls of the cubic simulation domain (Figure 3(a))

numbered **1**–**5**, define bulk solution conditions governed by equation 2:

$$C_i = C_{i,b} \qquad (2)$$

where $C_{i,b}$ is the bulk concentration of species *i*. Boundary **6** represents the inert basal plane and therefore there is no normal flux through the boundary, as described by:

$$\underline{n} \cdot D_i \nabla C_i = J_{\perp(hkl)} \qquad (3)$$

where $\underline{n}$ is the inward pointing unit normal to the surface. Boundaries **7**–**9** represent the etch pit walls on the (010), (001) and (100) crystal planes, respectively (Figure 3(b)) and their corresponding experimentally determined fluxes normal to specific planes, $J_{\perp(hkl)}$, (mol m^{-2} s^{-1}) were used as inputs for predicting concentration profiles, mass transport effects and the interfacial concentration (of Ca^{2+} or SO_4^{2-}) ions at each plane, as governed by:

$$\underline{n} \cdot D_i \nabla C_i = J_{\perp(hkl)} \qquad (4)$$

Results and Discussion

Etch pit characterisation and analysis

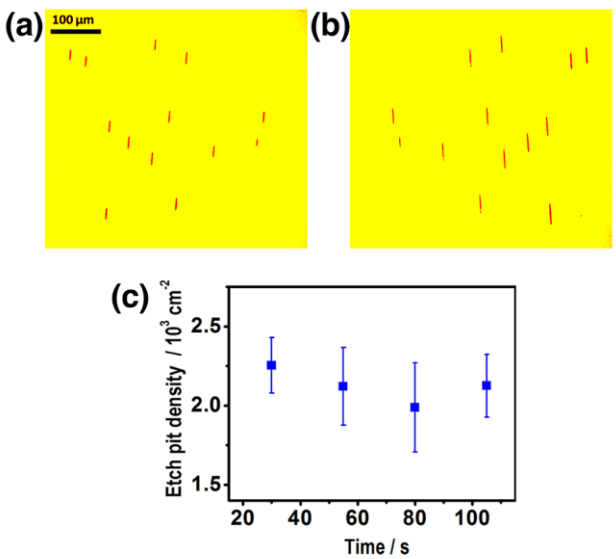

Fig. 4 DIC micrographs of the (010) surface of gypsum showing matched cleavage faces after etching for (a) 50 sec and (b) 100 sec etch in pure H_2O. Note the correspondence of etch pits on the same mirror positions. Etch pit density as a function of time is showing.

We have found that at short times (t < 200 s) in gypsum (010) surface dissolution, the dominant process is the formation and expansion of relatively deep pits. Such pits are known to generally nucleate at dislocation sites emerging at the surface.[18, 38] This is evident from Figure 4 which depicts DIC micrographs of matched cleavage faces etched for (a) 50 s and (b) 100 s. Although the two surfaces were etched for different times, so that the etch pits are larger in 4(b) than in (a), they evidently nucleate at the same (mirror) location on each surface. The correspondence of the etch pits is clear evidence that they emerge from dislocations which run through the crystal (essentially perpendicular to the (010) plane).[18a] For any specific etching duration and solution, etch pits of this type were formed across the entire surface and were found to exhibit similar dimensions to each other (within ≤ 10%). This indicated that pit formation for the (010) gypsum surface occurred via an essentially instantaneous process. Significantly, any particular pit is characteristic of the dissolution process at the time of observation. This is confirmed by Figure 4(c) which plots the etch pit density as a function of etching duration, revealing an essentially constant pit density. Such characteristic etch features occur generally in the dissolution of many crystalline materials[4b, 6, 18, 38] making the approach advocated here, where one characterises diffusionally isolated pits at specific times, widely applicable.

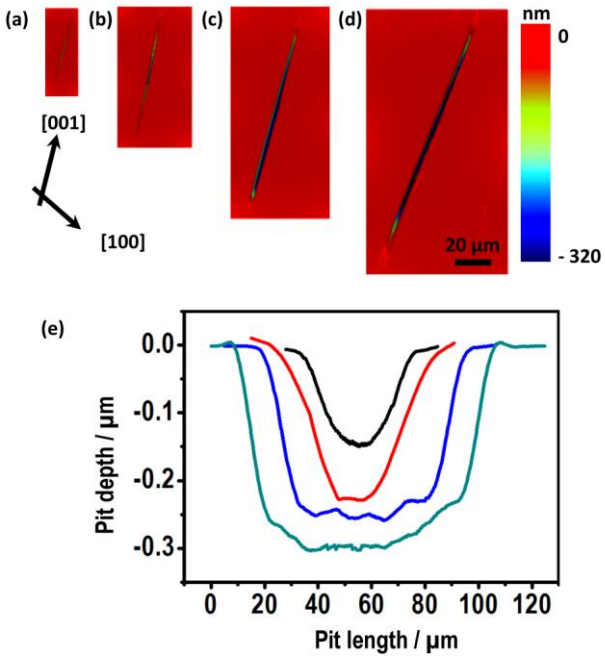

Fig. 5 Typical AFM micrographs of etch pits produced after etching the (010) gypsum surfaces in 0.2 M $NaNO_3$ solution for (a) 30 s, (b) 55 s, (c) 80 s, (d) 105 s and (e) corresponding cross-sectional profiles along the [001] direction for 30 s (black), 55 s (red), 80 s (blue) and 105 s (cyan). Note the evident anisotropy of step kinetics which results in etch pit elongation along the [001] direction. Pit depth corresponds to expansion dissolution perpendicular to the (010) face.

Figure 5 shows typical *ex-situ* AFM images of etch pits produced after etching the (010) plane of gypsum in 0.2 M $NaNO_3$ for (a) 30 s, (b) 55 s, (c) 80 s and (d) 105 s. For each time, a freshly cleaved surface was etched. The images show that as the etch pits evolve with time there is no significant change in morphology.

In this, and all cases, the etch pit shape resembles a parallelogram elongated along the [001] direction, with well-defined edges of the etch pit embracing the main [100] and [001] crystallographic directions (Figure 6). This trend in pit growth was typical, and the major (faceted) pit dimensions measured as a function of time, were used to produce direction-dependent dissolution rates and as inputs in simulations. To analyse the pits, we define a dissolution rate (velocity) normal to the main (010) surface $v_{(010)}$, which essentially corresponds to the rate of

nucleation of steps at the dislocation site.[18a] While one might expect different velocities at different defects, we found a rather narrow spread of such rates under the high driving conditions of our investigations. Lateral dissolution across the surface was measured in terms of the velocities of the main step orientations in the direction perpendicular to the step, i.e. $v_{\perp[100]}$ and $v_{\perp[001]}$ as illustrated schematically in Figure 3(c).)

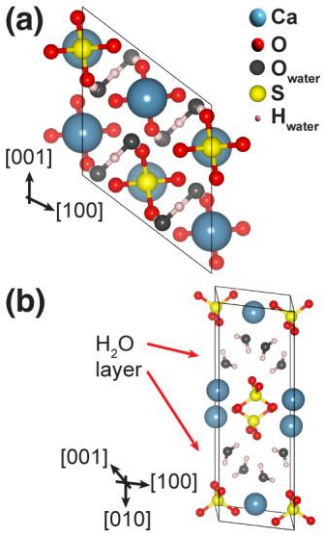

Fig. 6 (a) Atomic structure of the (010) surface of gypsum and (b) the unit cell with the interspaced H_2O layer shown.

The initially isolated pits tended to coalesce typically at times > 15 min in pure H_2O and > 10 min at IS = 0.2 M (in inert salt solution), which was well beyond the maximum duration used experimentally (≤ 105 ±3 s) for quantitative etch pit analysis. By focusing on short times we are able to consider the development of non-interacting etch pits and, moreover, on this length scale mass transport is strongly diffusional with negligible contribution from (natural) convective effects for the free-etched surfaces.

Etch pit depth, due to dissolution, perpendicular to the (010) plane, was typically in the range 50–530 nm (in pure H_2O), increasing as the etch time increased. The dimension of a characteristic repeat layer in this direction, comprising one $CaSO_4$ layer (Figure 6(b)) is ≈ 0.4 nm,[39] which suggests that even for the shortest dissolution period (30 ±3 s), the pits analysed were at least 120 monolayers deep. We note that previous *in-situ* AFM studies[31, 32] have mainly reported only the formation of shallow pits with depths of just a few monolayers. However, these latter measurements were made close to equilibrium over long time periods and targetted small areas of the crystal surface. Shallow etch features of this sort most likely emerge from point defects.

Step displacement kinetics and analysis

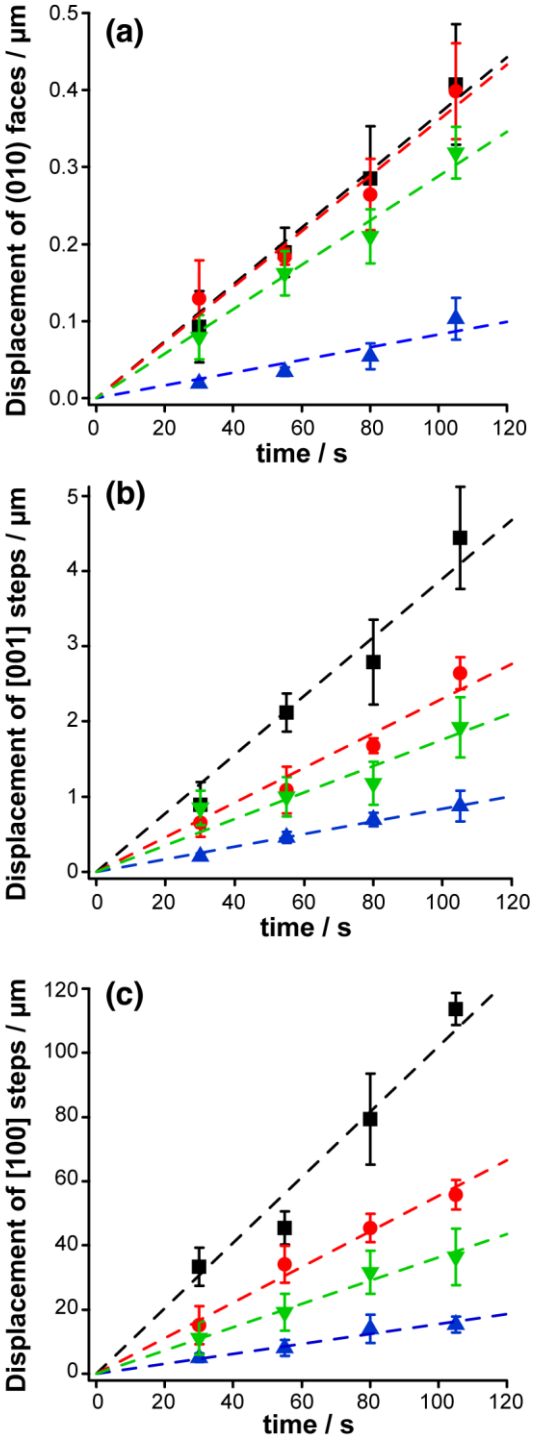

Fig. 7 Etch pit displacements as a function of etching time in solutions of 0.2 M $NaNO_3$ (black), 0.075 M Na_2SO_4 (red), $Ca(NO_3)_2 \cdot 4H_2O$ (blue) and pure H_2O (green): perpendicular to (a) (010) face, and velocities of (b) [001]-oriented steps and (c) [100]-oriented steps. The solid lines are linear fits to the experimental data.

Figure 7 shows summary plots of etch pit displacement as a function of time, perpendicular to the (010) face (a), and for the motion of [001]-oriented steps (b) and [100]-oriented steps (c). These data were obtained from direct measurement of pits via AFM, for all etching solutions used. Lateral measurements of pit expansion from the motion of the [001] and [100] steps were taken at 50% pit depth, while pit depths (dissolution

perpendicular to the (010) face) were determined from average pit depth, from the basal floor of the pit to the crystal basal surface. For each etching time, at least three surfaces were etched and, from these, at least three characteristic etch pits were analysed. The displacements plotted in Figure 7 are average values and the error bars represent two standard deviations. Reasonably linear relationships of displacement versus time were found for all directions. Directional dissolution velocities calculated from each of the slopes in Figure 7 are summarized in Table 1.

Table 1. Direction-specific displacement velocities from etch pit dissolution

Solution	Displacement velocities (nm s^{-1})		
	$v_{\perp[100]}$	$v_{\perp[001]}$	$v_{\perp(010)}$
H_2O	330 ±30	17 ±3	3.0 ±0.4
$NaNO_3$	1030 ±60	31 ±4	4.1 ±0.6
Na_2SO_4	550 ±30	20 ±3	3.7 ±0.5
$Ca(NO_3)_2{\cdot}4H_2O$	160 ±10	8.5 ±1.2	0.9 ±0.2

For etching in pure H_2O, there is a significant difference in step velocities: 330 ±30 nm s^{-1} and 17 ±3 nm s^{-1} for the [100] and [001] steps, respectively. This order of dissolution velocities can be rationalized to some extent by reference to bonding in the crystal, particularly within the $CaSO_4$ bilayer (Figure 6(b)), as outlined by Teng and Fan,[31] essentially using periodic bond chain arguments.[39] We do not seek to repeat their arguments here, but point out the main features. In the 2 layers that form the $CaSO_4$ bilayer, like charges in each layer are in a staggered conformation with respect to each other along the [001] direction, while along the [100] direction, like-ions are in an eclipsed conformation when comparing the atom arrangement in each layer. Consequently, each Ca^{2+} ion neighbours 3 SO_4^{2-} in the [001] direction, but only 2 SO_4^{2-} in the [100] direction. Furthermore, the smaller distance between nearest Ca^{2+} in the [001] direction compared to the [100] direction indicates a higher atom density and suggests a more stable step, as seen in dissolution experiments. Dissolution perpendicular to the (010) face was characterized by an effective velocity of 3.0 ±0.4 nm s^{-1}. In this direction, a H_2O layer is sandwiched between the $CaSO_4$ layers through H-bonding[40] (Figure 6(b)) thereby disrupting the continuity of the periodic bond chain in this direction).

Compared to dissolution in pure H_2O, etching in 0.2 M $NaNO_3$ was found to enhance step velocities (salting-in)[14a, 41] by factors of ≈ 3 and ≈ 2 for the [100] and [001] steps. In contrast, dissolution perpendicular to the (010) face was less affected, with a velocity a factor ≈ 1.3 of the value in pure water. The enhanced dissolution rates are expected since gypsum solubility increases by a factor of 2 from C_{sat} = 16.2 mM in pure H_2O to C_{sat} = 32.3 mM (MINEQL+) with 0.2 M $NaNO_3$. However, it is evident that the salt effect is strongly direction-dependent, impacting dissolution for the fast moving [100] step, in particular. This highlights a powerful feature of the methodology described: the ability to readily identify microscopic differences for common processes such as salting-in. Such effects have rarely been examined at the microscopic level and are opened up for scrutiny with the methodology described herein.

Conversely, dissolution in solutions containing common ions (Na_2SO_4 and $Ca(NO_3)_2{\cdot}4H_2O$ solutions) yielded strikingly different velocity trends, despite having similar IS values. Naturally, compared to etching at the same IS with an inert supporting electrolyte ($NaNO_3$), dissolution velocities in all directions are predictably lower for both Na_2SO_4 and $Ca(NO_3)_2{\cdot}4H_2O$ (common ion effect). However, from Figure 7 and Table 1, it is evident that dissolution velocities in the presence of SO_4^{2-} ions are significantly higher than values obtained in the Ca^{2+}-rich solution for all directions. This observation is particularly striking for dissolution perpendicular to the (010) face of the pit (Figure 7(a)) where dissolution velocities are more than 4 times higher when etching occurs in the presence of SO_4^{2-} ion compared to Ca^{2+}. These effects can be rationalized generally, because gypsum crystal exhibits a negative ζ-potential in pure H_2O under standard conditions and over a wide pH range.[42] Thus, in a Ca^{2+}-rich solution, the back reaction, characterized by the adsorption of Ca^{2+} (and SO_4^{2-}) on the crystal surface, appears to be enhanced compared to the situation in the SO_4^{2-}-rich solution.

When comparisons can be made to previous studies, the step displacement velocities deduced in this work are higher than those deduced by *in-situ* AFM. It is also evident from reviewing the literature that AFM has provided a rather wide range of kinetic data, hitherto, even under apparently similar conditions. Thus, at a relative saturation, $S = C/C_{sat}$ = 0.65, where C is the bulk solution concentration, Bosbach and Rammensee[32a,b] measured velocities of steps running parallel to the [100] and [001] directions of ≤ 30.0 nm s^{-1} and ≤ 2.5 nm s^{-1}, respectively. While these values were later corroborated,[32] Fan and Teng [31] deduced much slower step velocities for steps parallel to [100], in the range of 7 nm s^{-1} (for lower S = 0.34, i.e. higher driving force) to 2 nm s^{-1} (at higher S = 0.96), while steps parallel to [001] moved at ≈ 1.2 nm s^{-1} (at lower S) to 0.2 nm s^{-1} (at higher S). Most recently, Pachon-Rodriguez *et al.*,[43] have reported even lower step velocities of < 1 nm s^{-1} for steps parallel to the [100] and [001] directions over the entire range of S ≈ 0.2 – 0.95 and also pointed out how the applied force in AFM can greatly influence kinetics measurements. It is evident from this analysis and previous AFM results that step velocities vary by much more than 1 order of magnitude, even under similar undersaturation conditions.

At first glance, one might attribute the difference between our measurements and previous AFM studies[31-32, 43] to the fact that AFM has to be conducted at medium to low driving force to deliberately slow the step movement (*vide supra*). However, if one extrapolates between previous AFM results and our measurements at high driving force, using common rate laws, such as first or higher order dependences of dissolution on (interfacial) undersaturation, then the rates we measure are still higher. Because our measurements show step dissolution kinetics to be very fast, one can reasonably posit that mass transport effects are a major limiting factor in the *in-situ* AFM environment. Our studies show that the gypsum surface becomes

fully reactive in ca. 15 mins at extreme undersaturated conditions. While this time scale will lengthen approaching saturation, the long duration of typical AFM measurements due to the need for thermal equilibration before measurements are made and slow acquisition times, means that the entire gypsum surface is subject to (slow and limiting) planar diffusion with a characteristic diffusion boundary layer of 200 – 500 µm.[44] As such, there would be considerable (complete) diffusional cross-talk between neighbouring steps and neighbouring sites across large lateral length scales, and step velocities would be linked intimately to step density.

In contrast, as we further elaborate below, and we highlighted earlier when discussing our methodology, by studying dissolution under conditions where only microscale features are active on an inert surface means that high mass transport rates are delivered to reactive sites. This methodology thus reveals faster intrinsic rates, just as micro-electrodes and nano-electrodes have allowed the exploration of faster surface kinetics compared macroscale measurements.[22, 23]

Direction-Specific Dissolution Kinetics

Dissolution fluxes normal to specific crystal faces, $J_{\perp(hkl)}$, (mol m^{-2} s^{-1}) were calculated as the product of experimentally deduced dissolution velocities, and the molar density (13400 mol m^{-3}) of the crystal.[45] These values are summarised in Table 2 and predictably mirror the trend seen in the displacement velocity measurements (*vide supra*) such that $J_{\perp(010)} < J_{\perp(001)} << J_{\perp(100)}$.

Table 2. Summary of plane specific fluxes.

Solution	Flux (mol m^{-2} s^{-1}) normal to plane		
	$J_{\perp(100)}$	$J_{\perp(001)}$	$J_{\perp(010)}$
H_2O	5.1 (±0.5) $\times10^{-3}$	2.5 (±0.4) $\times10^{-4}$	4.0 (±0.5) $\times10^{-5}$
$NaNO_3$	1.6 (±0.1) $\times10^{-2}$	4.7 (±0.5) $\times10^{-4}$	5.5 (±0.8) $\times10^{-5}$
Na_2SO_4	8.4 (±0.4) $\times10^{-3}$	3.1 (±0.4) $\times10^{-4}$	5.0 (±0.7) $\times10^{-5}$
$Ca(NO_3)_2{\cdot}4H_2O$	2.4 (±0.2) $\times10^{-4}$	1.3 (±0.2) $\times10^{-4}$	1.2 (±0.3) $\times10^{-5}$

These direction-specific dissolution fluxes were used in conjunction with the etch pit dimensions as $Ca(NO_3)_2{\cdot}4H_2O$ inputs for the finite element model which predicted the corresponding (Ca^{2+} and SO_4^{2-}) concentration profiles around the pits and, in particular, the interfacial concentration of dissolved Ca^{2+} and SO_4^{2-} at reactive pit faces. From these profiles, the relative importance of mass transport and surface kinetics was elucidated, from which the kinetic (rate-determining) regime could be determined.

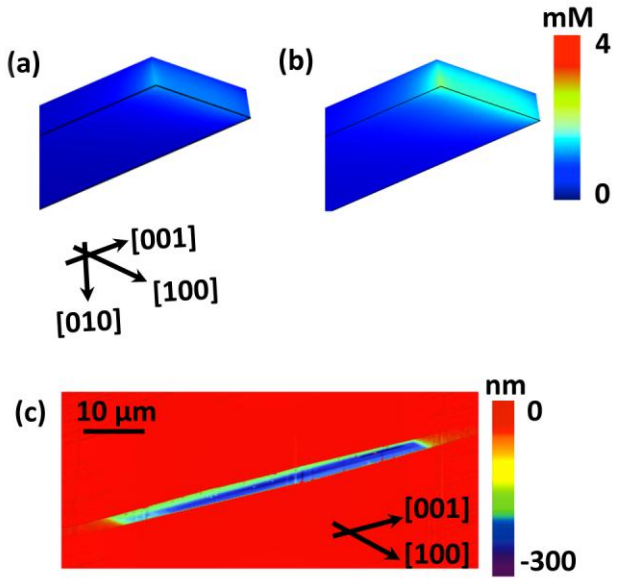

Fig. 8 Typical simulated interfacial Ca^{2+} (and SO_4^{2-}) concentration profile over a pit surface, from a section of the overall pit (not to scale) focusing on the (100) face, after (a) 50 and (b) 100 s of dissolution in pure H_2O. For comparison (c) is an experimental etch pit formed after 100 s etch in pure H_2O viewd by VSI. The magnification (a-b) highlights the change in surface concentration on the fast moving (100) face.

Figure 8 illustrates a section of an overall simulated pit, approximated reasonably well as a cuboid (*vide supra*). The pit profile is shown at times of (a) 50 s and (b) 100 s in pure H_2O. For each specific time, it is evident that the surface concentration profile is heterogeneous over the pit surface, with the highest concentration arising from the fast moving (100) face. At the mid-time in the process (50 s, Figure 8(a)), it was found that the total average interfacial concentration was 0.17 mM, 0.18 mM and 0.88 mM for the (010), (001) and (100) faces, respectively. The highest interfacial concentration (on the (100) face) equates to ≈ 5.4% C_{sat} indicating that, on this scale, dissolution is essentially controlled by surface kinetics. This is a direct consequence of high mass transport from a microscopically active surface mentioned above. At later times in the dissolution process (100 s, Figure 8(b)), the surface concentration values increase (as the pit dimensions increase) to such an extent that surface to bulk diffusion becomes more important, particularly for dissolution of the (100) face. Nonetheless, the regime is still far from diffusion-control. Note that even using a fast flow channel cell we were unable to measure the intrinsic surface dissolution kinetics for the (001) surface due to mass transport limitations.[30] The fact that we can measure intrinsic kinetics for both the (001) plane and even faster dissolving (100) plane highlights the power of the approach presented, and is a direct consequence of the high intrinsic diffusion rates to microscale reactive features on the surface.

Linking microscopic and macroscopic dissolution kinetics

The average rate (in pure H_2O) of dissolution from the entire etch pit was predicted from simulations, by summing the fluxes over the pit surface, $J = 1.34 \times10^{-4}$ mol m^{-2} s^{-1} and $J = 1.27 \times10^{-4}$

mol m^{-2} s^{-1} for dissolution after 50 s and 100 s, respectively. When the relative surface area of individual faces, $A_{(hkl)}$ is considered, these rates suggest that gypsum dissolution at early times (≤ 100 s) is dominated by the edge (100) and (001) planes relative to the basal (010) surface. These average rates decrease with time as a consequence of pit expansion, such that the face area ratios, $A_{(100)}/A_{(010)}$ (and similarly $A_{(001)}/A_{(010)}$), decrease significantly as a function of etching duration and, consequently, the contributions from these high flux faces diminish over time. Eventually, at longer times (where the surface is fully reactive) dissolution is dominated by the nucleation of new steps at the basal plane. Under these conditions, the flux from the basal plane is predicted to be $J_{\perp(010)}$ = 4.0 (±0.5) ×10^{-5} mol m^{-2} s^{-1} which is in good agreement with both our recently measured value[30] and the value suggested by Colombani,[30] who reviewed various previous bulk studies and deduced J = 5 (±2) ×10^{-5} mol m^{-2} s^{-1} [33] by extrapolation of the mass transport rates of many different techniques. The fact that our microscale and nanoscale measurements relate accurately to the bulk dissolution rate provides confidence in our method: we bridge the gap between microscopic phenomena and macroscopic rates. In contrast, AFM measurements[31, 32] are not consistent with macroscopic rates.[29, 30]

In light of the work herein, it is evident that the overall flux deduced from macroscopic measurements will necessarily be very sensitive to the microscopic nature of the surface exposed, with [100] and [001] steps and facets, in particular, providing significant local fluxes. Our studies, with the deduction of plane-specific and step-specific dissolution kinetics, provides a true value for the dissolution of the (010) surface and a framework for the construction of accurate dissolution models for complex (polycrystalline) materials and single crystal surfaces that might exhibit an abundance of different microfacets. Furthermore, knowledge of intrinsic dissolution kinetics for specific planes and steps, also makes it possible to predict the relative importance of mass transport for different measurement techniques and situations, taking full account of the nature of the exposed gypsum material.

Conclusions

We have described a method for the analysis of characteristic etch pits formed by dissolution of crystal surfaces, that allows microscopic surface kinetics to be deduced, free from diffusional limitations, and linked to macroscopic fluxes in a self-consistent manner. The methodology provides a quantitative interpretation of the relative importance of surface kinetics compared to mass transport in controlling dissolution rates at different crystal facets (steps, planes).

An important aspect of the analysis is that direction-specific reaction rates are deduced directly. For the case of gypsum, at early times in the process, dissolution in all measured directions was predominantly surface-controlled, but the fast moving steps parallel to the [100] direction yielded higher interfacial local concentrations, indicating relatively more limitations from mass transport, which became increasingly important with time (but still a small component on the time and length scale of the measurements herein). The etch pit morphology was dominated by the large flat (010) pit base for which the normal dissolution flux was $J_{\perp(010)}$ = 4.0 (±0.5) ×10^{-5} mol m^{-2} s^{-1}. This value compares well with previous macroscopic flux measurements of this face. Past attempts to measure intrinsic fluxes from other faces (edge planes) have been unsuccessful due to the fast dissolution rates which have simply been controlled by mass transport. Herein, we have measured these fluxes for the first time and find $J_{\perp(001)}$ = 2.5 (±0.4) ×10^{-4} mol m^{-2} s^{-1} and $J_{\perp(100)}$ = 5.1 (±0.5) ×10^{-3} mol m^{-2} s^{-1}. The associated step velocities are faster than measured by *in-situ* AFM studies which are highly likely to be impacted by mass transport limitations. Moreover, as highlighted herein, published AFM measurements of gypsum dissolution are not self-consistent.

Studies of salt effects have yielded two important new observations for gypsum. First, the addition of an inert salt ($NaNO_3$) results in faster dissolution velocities for all major crystal facets compared to dissolution in pure water, but the magnitude of the salt effect is direction-specific. Second, a brief exploration of common ion effects (Ca^{2+} vs. SO_4^{2-} in bulk solution) has revealed a significant retardation effect of Ca^{2+} ion compared to SO_4^{2-}. This has been rationalized, partly, based on the known (negative) ζ-potential of gypsum, but there are again direction-specific influences. In future studies, it would be interesting to understand the origins of these directional effects, through further microscopic characterization and modelling.

Acknowledgements

This work was supported by the European Research Council (funding for P.R.U., M.P. and M.M.M.). We also thank St-Gobain Gyproc for some initial funding for M.M.M., and the EPSRC-funded MOAC doctoral training centre (funding for M.A.E). Some of the equipment used in this research was obtained through Birmingham Science City with support from Advantage West Midlands and the European Regional Development Fund.

Notes and references

1. P. R. Unwin and J. V. Macpherson, *Chem. Soc. Rev.*, 1995, **24**, 109-119.
2. A. C. Lasaga, *Kinetic Theory and Applications in Earth Sciences*, Princeton Press, Princeton, 1998.
3. a) R. Tang, G. H. Nancollas and C. A. Orme, *J. Am. Chem. Soc.*, 2001, **123**, 5437-5443. b) G. H. Nancollas, *Biological Mineralization and Demineralization*, Springer-Verlag, Berlin, 1982. c) W. Stumm, *Chemistry of the Solid-Water Interface*, Wiley, New York, 1992. d) A. I. Vavouraki, C. V. Putnis, A. Putnis and P. G. Koutsoukos, *Chem. Geol.*, 2008, **253,** 243-251. e) J. Chen, B. Sarma, J. M. B. Evans and A. S. Myerson, *Cryst. Growth Des.*, 2011, **11**, 887-895.
4. a) A. Lüttge, *J. Electron. Spectrosc. Relat. Phenom.*, 2006, **150**, 248-259. b) A. C. Lasaga and A. Lüttge, *Science*, 2001, **291**, 2400-2404.
5. a) C. E. Jones, J. V. Macpherson and P. R. Unwin, *J. Phys. Chem. B*, 2000, **104**, 2351-2359. b) C. E. Jones, P. R. Unwin and J. V. Macpherson, *ChemPhysChem*, 2003, **4**, 139-146. c) R. Tang, *Prog. Chem.*, 2005, **17**, 368-376. d) R. Tang, C. A. Orme and G. H. Nancollas, *ChemPhysChem*, 2004, **5**, 688-696. e) L. Wang, R. Tang, T. Bonstein, C. A. Orme, P. J. Bush and G. H. Nancollas, *J. Phys. Chem. B*, 2004, **109**, 999-1005. e) E. H. Chow, D. K. Bučar and W. Jones, *Chem. Commun.*, 2012, **48,** 9210-26. f) T. Fujiwara, Y. Suzuki and K. Tamura, *J. Cryst. Growth*, 2011, **334,** 134-137. g) R. S. Abendan and J. A. Swift, *Cryst. Growth Des.*, 2005, **5,** 2146-2153.
6. J. W. Morse and R. S. Arvidson, *Earth-Sci. Rev.*, 2002, **58**, 51-84.
7. A. A. Jeschke and W. Dreybrodt, *Geochim. Cosmochim. Acta*, 2002, **66**, 3055-3062.
8. J. W. Zhang and G. H. Nancollas, *Rev. Mineral.*, 1990, **23**, 365-396.

9. H. Singh and M. Bajwa, *Soil Res.*, 1990, **28**, 947-953.
10. I. N. MacInnis and S. L. Brantley, *Chem. Geol.*, 1993, **105**, 31-49.
11. a)K. Burns, Y.-T. Wu and C. S. Grant, *Langmuir*, 2003, **19**, 5669-5679. b) C. A. Brown, R. G. Compton and C. A. Narramore, *J. Colloid Interface Sci.*, 1993, **160**, 372-379. c) R. G. Compton and P. J. Daly, *J. Colloid Interface Sci.*, 1987, **115**, 493-498.d) S.-T. Liu and G. H. Nancollas, *J. Inorg. Nucl. Chem.*, 1971, **33**, 2311-2316. e) U. Svensson and W. Dreybrodt, *Chem. Geol.*, 1992, **100**, 129-145.
12. a) P. R. Unwin, A. J. Barwise and R. G. Compton, *J. Colloid Interface Sci.*, 1989, **128**, 208-222. b) R. G. Compton, K. L. Pritchard and P. R. Unwin, *Chem. Commun.*, 1989, 249-251. c) R. G. Compton and P. R. Unwin, *Phil. Trans. R. Soc. A*, 1990, **330**, 1-45. d) R. Orton and P. R. Unwin, *J. Chem. Soc., Faraday Trans.*, 1993, **89**, 3947-3954. e) Q. Hong, M. F. Suárez, B. A. Coles and R. G. Compton, *J. Phys. Chem. B*, 1997, **101**, 5557-5564. f) L. Peltonen, P. Liljeroth, T. Heikkilä, K. Kontturi and J. Hirvonen, *Eur. J. Pharm. Sci.*, 2003, **19**, 395-401.
13. P. M. Dove and F. M. Platt, *Chem. Geol.*, 1996, **127**, 331-338.
14. a) G. Binnig, C. F. Quate and C. Gerber, *Phys. Rev. Lett.*, 1986, **56**, 930-933. b) E. Ruiz-Agudo, M. Urosevic, C. V. Putnis, C. Rodríguez-Navarro, C. Cardell and A. Putnis, *Chem. Geol.*, 2011, **281**, 364-371. c) G. Jordan and W. Rammensee, *Geochim. Cosmochim. Acta*, 1998, **62**, 941-947. d) E. H. Chow, D. K. Bučar and W. Jones, *Chem. Commun.*, 2012, **48,** 9210-26. e) J. Cama, L. Zhang, J. M. Soler, G. D. Giudici, R. S. Arvidson and A. Lüttge, *Geochim. Cosmochim. Acta*, 2010, **74,** 4298-4311. f) E. Ruiz-Agudo, M. Kowacz, V. Putnis and A. Putnis, *Geochim. Cosmochim. Acta*, 2010, **74,** 1256-1267.
15. a) J. V. Macpherson and P. R. Unwin, *J. Phys. Chem.*, 1995, **99**, 14824-14831. b) J. V. Macpherson, P. R. Unwin, A. C. Hillier and A. J. Bard, *J. Am. Chem. Soc.*, 1996, **118**, 6445-6452. c) C.A. McGeouch, M. Peruffo, M. A. Edwards, L. Dexter, R. Lazenby, M. M. Mbogoro, K. McKelvey and P. R.Unwin, J. Phys. Chem. C, 2012, **116**, 14892-14899. d) J. V. Macpherson and P. R. Unwin, *J. Phys. Chem.*, 1995, **99**, 3338-3351. e) J. V. Macpherson and P. R. Unwin, *J. Phys. Chem.*, 1994, **98**, 1704-1713.
16. A. Lüttge, E. W. Bolton and A. C. Lasaga, *Am. J. Sci.*, 1999, **299**, 652-678.
17. a) D. Gasperino, A. Yeckel, B. K. Olmsted, M. D. Ward and J. J. Derby, *Langmuir*, 2006, **22**, 6578-6586. b) D. P. Burt, N. R. Wilson, U. Janus, J. V. Macpherson and P. R. Unwin, *Langmuir*, 2008, **24**, 12867-12876.
18. a) K. Sangwal, *Etching of Crystals, Theory, Experiment and Application*, North Holland, Amsterdam, 1987. b) A. E. Blum and A. C. Lasaga, *Aquatic Surface Chemistry*, John Wiley, New York, 1987.
19. a) S. L. Brantley, J. D. Kibicki and A. F. White, *Kinetics of Water-rock Interaction*, Springer Science, New york, 2008. b) A. E. Blum, R. A. Yund and A. C. Lasaga, *Geochim. Cosmochim. Acta*, 1990, **54**, 283-297.
20. a) R. S. Arvidson, I. E. Ertan, J. E. Amonette and A. Lüttge, *Geochim. Cosmochim. Acta*, 2003, **67**, 1623-1634. b) J. Cama, L. Zhang, J. M. Soler, G. D. Giudici, R. S. Arvidson and A. Lüttge, *Geochim. Cosmochim. Acta*, 2010, **74**, 4298-4311.
21. a) R. C. Engstrom, T. Meaney, R. Tople and R. M. Wightman, *Anal. Chem.*, 1987, **59**, 2005-2010. b) J. Heinze, *Angew. Chem.*, 1993, **32**, 1268-1288. c) G. Taylor and H. H. J. Girault, *J. Electroanal. Chem.*, 1986, **208**, 179-183. d) M. Fleischmann, F. Lasserre, J. Robinson and D. Swan, *J. Electroanal. Chem.*, 1984, **177**, 97-114. e) R. M. Wightman, *Science*, 1988, **240**, 415. f) J. O. Howell and R. M. Wightman, *Anal. Chem.*, 1984, **56**, 524-529.
22. R. J. Forster, *Chem. Soc. Rev.*, 1994, **23**, 289-297.
23. A. J. Bard and L. R. Faulkner, *Electrochemical Methods: Fundamentals and Applications*, John Wiley & Sons, Inc., USA, New York, 2001.
24. D. C. Ford and P. W. William, *Karst Geomorphology and Hydrology*, Unwin Hyman, 1989.
25. G. M. Van Rosmalen, P. J. Daudey and W. G. J. Marchée, *J. Cryst. Growth*, 1981, **52**, 801-811.
26. J. Alonso-Azcárate, S. H. Bottrell and J. Tritlla, *Chem. Geol.*, 2001, **174**, 389-402.
27. J. Alonso-Azcárate, S. H. Bottrell and J. R. Mas, *Chem. Geol.*, 2006, **234**, 46-57.
28. D. Bosbach and M. F. Hochella Jr, *Chem. Geol.*, 1996, **132**, 227-236.
29. a) J. Christoffersen and M. R. Christoffersen, *J. Cryst. Growth*, 1976, **35**, 79-88. b) A. A. Jeschke, K. Vosbeck and W. Dreybrodt, *Geochim. Cosmochim. Acta*, 2001, **65**, 27-34. c) J. Colombani and J. Bert, *Geochim. Cosmochim. Acta*, 2007, **71**, 1913-1920.
30. M. M. Mbogoro, M. E. Snowden, M. A. Edwards, M. Peruffo and P. R. Unwin, *J. Phys. Chem. C*, 2011, **115**, 10147-10154.
31. C. Fan and H. H. Teng, *Chem. Geol.*, 2007, **245**, 242-253.
32. a) D. Bosbach, D. G. Jordan and W. Rammensee, *Eur. J. Mineral.*, 1995, **7**, 267-276. b) D. Bosbach and W. Rammensee, *Geochim. Cosmochim. Acta*, 1994, **58**, 843-849. c) C. Hall and D. C. Cullen, *AlChE J.*, 1996, **42**, 232-238.
33. J. Colombani, *Geochim. Cosmochim. Acta*, 2008, **72**, 5634-5640.
34. W. D. Schecher, *A Chemical Equilibrium Modeling System*, Hallowell, Maine, 2003.
35. F. M. Morel and J. G. Hering, *Principles and Applications of Aquatic Chemistry*, Wiley, New York, 1993.
36. C.-A. McGeouch, M. A. Edwards, M. M. Mbogoro, C. Parkinson and P. R. Unwin, *Anal. Chem.*, 2010, **82**, 9322-9328.
37. P. Vanysek, *CRC Handbook of Chemistry and Physics*, CRC Press Taylor & Francis, Boca Raton, FL, 2010-2011.
38. a) A. F. White and S. L. Brantley, *Rev. Mineral. Geochem.*, 1995, **31**, 1-22. b) A. Lüttge, *Am. Mineral.*, 2005, **90**, 1776-1783.
39. P. F. Schofield, K. S. Knight and I. C. Stretton, *Am. Mineral.*, 1996, **81**, 847-851.
40. P. Hartman and W. G. Perdok, *Acta Crystallographica*, 1955, **8**, 521-524.
41. a) M. Kowacz and A. Putnis, *Geochim. Cosmochim. Acta*, 2008, **72**, 4476-4487. b) E. Ruiz-Agudo, M. Kowacz, C. V. Putnis and A. Putnis, *Geochim. Cosmochim. Acta*, 2010, **74**, 1256-1267.
42. a) A. S. Buchanan and E. Heymann, *J. Colloid Sci.*, 1949, **4**, 137-150. b) S. Titiz-Sargut, P. Sayan and B. Avci, *Cryst. Res. Technol.*, 2007, **42**, 119-126.
43. E. A. Pachon-Rodriguez, A. Piednoir and J. Colombani, *Phys. Rev. Lett.*, 2011, **107**, 146102.
44. a) A. E. S. Van Driessche, J. M. Garci a-Ruiz, J. M. Delgado-Lopez and G. Sazaki, *Cryst. Growth Des.*, 2010, **10**, 645-682. b) V. G. Levich, *Physicochemical hydrodynamics*, Prentice-Hall, 1962.
4. G. R. Olhoeft and G. R. Johnson, in *Practical Handbook of Physical Properties of Minerals*, ed. R. S. Carmichael, CRC Press, Boca Raton, Florida, 1989.